nature communications

Article

https://doi.org/10.1038/s41467-026-74500-3

Electrode-free bioelectrochemical intercalation for scalable lithium recovery

Received: 27 March 2026

Accepted: 8 June 2026

Published online: 29 June 2026

Check for updates

Kohei Shimokawa [1,2,3,11] ✉, Duyen Minh Pham[3,4,11], Heng Yi Teah[5], Xizi Long [3], Yasunori Kikuchi [5,6,7] ✉ & Akihiro Okamoto [3,4,8,9,10] ✉

Electrochemical intercalation materials offer selective lithium recovery from saline streams, but conventional electrode architectures impose scale-up constraints. Here we report an electrode-free bioelectrochemical intercalation process in which a dissimilatory metal-reducing bacterium, *Shewanella oneidensis* MR-1, drives lithium uptake into λ-MnO_2. The system self-assembles into microbe–mineral agglomerates that sustain electrochemical-rate intercalation without external wiring, forming a recoverable lithiated slurry. Over 95% of lithium was recovered from seawater within hours, with less than 1% co-intercalation of competing metal ions. Bottom-up self-agglomeration, in which extracellular and cell-surface cytochromes facilitate efficient electron transfer, enables scale-up. The generality and energetic basis of this mechanism are further supported by reproducing the key behaviour in an orthogonal $FePO_4$ host with negligible abiotic reactivity. Techno-economic and life-cycle analyses for Li_2CO_3 production suggest that the process reduces brine water loss while maintaining competitive costs. These results establish self-assembled bioelectrochemical intercalation as a route to lithium recovery from saline streams.

Li, an essential component of rechargeable batteries, is pervasive in nature, yet its distribution exhibits considerable heterogeneity[1–8]. Historically, the exploitation of high-concentration Li reserves, such as brines and ores, has been the primary focus. However, the escalating global demand for large-scale Li-ion batteries (LIBs) has exposed the constraints of regional availability and the detrimental environmental repercussions associated with conventional evaporative Li recovery from brines and ore refining[3,9,10]. Consequently, there is a burgeoning need to develop environmentally benign Li recovery methods that demonstrate improved energy efficiency and enable the utilization of diverse Li sources[1–3,10,11]. Among the various alternative approaches, electrochemical techniques employing electrode materials for LIBs, such as λ-MnO_2 and $FePO_4$, demonstrate remarkable ability for rapid and selective Li recovery from sources with a range of concentrations, including low-concentration seawater (Supplementary Table 1)[5,11–22]. However, inherent limitations associated with two-dimensional electrode fabrication, including mass loading of electroactive material and ohmic drop, pose challenges to the scale-up of efficient and sustainable electrochemical Li recovery systems[1,3–6].

Dissimilatory metal-reducing bacteria are ubiquitous in low-oxygen marine and freshwater environments[23,24]. These bacteria couple anaerobic respiration of organic compounds linked to the

[1]Frontier Research Institute for Interdisciplinary Sciences, Tohoku University, Sendai, Japan. [2]Institute for Materials Research, Tohoku University, Sendai, Japan. [3]International Center for Materials Nanoarchitectonics (WPI-MANA), National Institute for Materials Science, Tsukuba, Japan. [4]Research Center for Macromolecules and Biomaterials, National Institute for Materials Science, Tsukuba, Japan. [5]Presidential Endowed Chair for "Platinum Society", The University of Tokyo, Tokyo, Japan. [6]Department of Chemical System Engineering, The University of Tokyo, Tokyo, Japan. [7]Institute for Future Initiatives, The University of Tokyo, Tokyo, Japan. [8]Graduate School of Chemical Sciences and Engineering, Hokkaido University, Sapporo, Japan. [9]Graduate School of Science and Technology, University of Tsukuba, Tsukuba, Japan. [10]Research Center for Autonomous Systems Materialogy, Institute of Integrated Research, Institute of Science Tokyo (Science Tokyo), Yokohama, Kanagawa, Japan. [11]These authors contributed equally: Kohei Shimokawa, Duyen Minh Pham. ✉e-mail: kohei.shimokawa.b7@tohoku.ac.jp; ykikuchi@ifi.u-tokyo.ac.jp; okamoto.akihiro@nims.go.jp

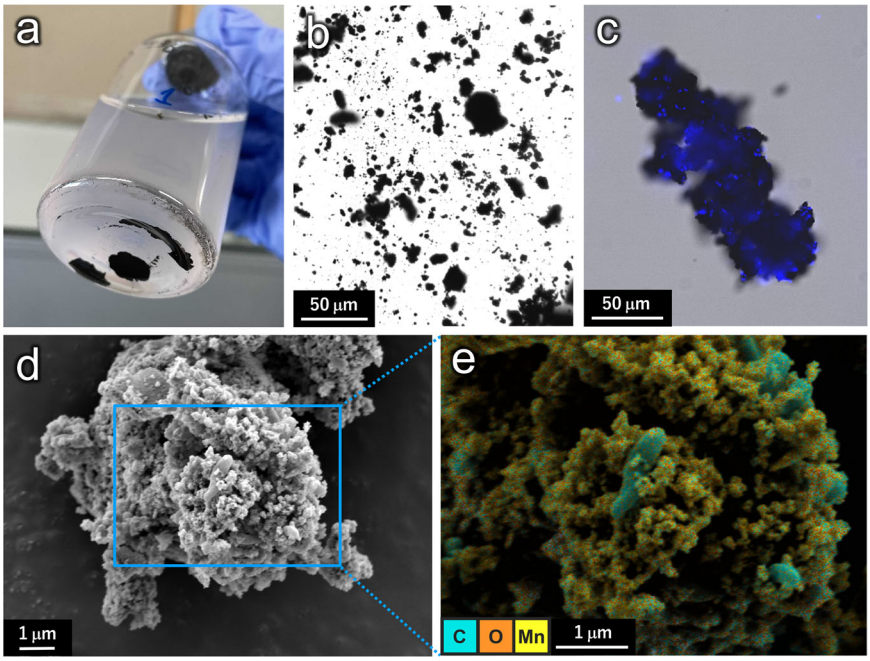


Fig. 1 | Self-agglomeration of *Shewanella oneidensis* MR-1 and λ-MnO_2 nanoparticles. a Agglomeration occurring at the bottom of the reactor after bioelectrochemical Li recovery in 50 mM LiCl/PBS solution with 50 mM lactate. **b** Microscopic image of the resuspended precipitate. **c** Fluorescent microscopy image of an agglomerate with DNA-stained MR-1 cells prepared via DAPI staining. **d** SEM and (**e**) EDS mapping images for a small piece of agglomerate formed in LiCl/PBS. Similar micrographic results were obtained in at least two independent experiments.

electrochemical reduction of extracellular electron acceptors via extracellular electron transfer (EET)[23,25]. EET-capable bacteria, such as *Shewanella oneidensis* MR-1, actively attach to the surface of nano-sized metal oxides and connect them with the extracellular or cell-surface enzymes to increase the mineral reduction rate[26–28]. Given the remarkable ability of these microbes to reduce metal oxides, EET could be a promising driving force to electrochemically recover Li without using electrodes. To date, EET has primarily been employed for modifying the oxidation state of several transition metals (*e.g.*, Cr, Mn, Fe, and Co)[29–31], leaving the manipulation of alkali and alkaline-earth metals unexplored.

In this study, we examine bioelectrochemical intercalation, wherein dissolved Li ions intercalate into a Li-ion sieve material accompanied by electron donation from microbes (Supplementary Fig. 1). Using this approach, we demonstrate the feasibility of bioelectrochemical Li recovery from artificial Li solutions and real seawater. Furthermore, we evaluate biological mechanisms, cost performance, and environmental impact to assess the scalability of our method.

Results

MR-1 drives electrode-free Li intercalation

Manganese oxides are biocompatible electron acceptors under anaerobic conditions for MR-1 and other EET-capable bacteria[27,32,33]. λ-MnO_2 with a spinel structure was chosen from the reported Li-ion sieve materials considering the high Li selectivity due to the three-dimensional diffusion path (Supplementary Fig. 2); its channels are small enough to prevent the intercalation of other metals that abundantly exist in brines and seawater (*e.g.*, Na^+, K^+, and Ca^{2+})[5,9]. Furthermore, the lithiation potential of λ-MnO_2 is substantially higher compared to other MnO_2 polymorphs (Supplementary Fig. 3)[34], resulting in a large driving force for Li intercalation.

We first examined Li recovery from LiCl solutions dissolved in phosphate-buffered saline (PBS) at pH 7.4 and at high concentrations of Na^+ and K^+. The synthesized λ-MnO_2 nanoparticles, whose lattice constant was determined to be ~8.037 Å (Supplementary Fig. 4), and MR-1 were anaerobically incubated with 50 mM LiCl/PBS in the presence of lactate as the electron donor for 24 h at 30 °C. Contrary to the expectation that bacterial EET would promote MnO_2 dissolution[27], the λ-MnO_2 nanoparticles remained in a solid state and self-organized into sheet-like precipitates (Fig. 1a). Upon mild resuspension, 10–50 μm agglomerates were observed (Fig. 1b), approximately 100 times larger than the initial nanoparticle size (Supplementary Fig. 5). Bacterial cells were intimately associated with the mineral matrix and further integrated them into >100 μm structure, as confirmed by fluorescence microscopy of DNA-stained MR-1 (Fig. 1c) and SEM–EDS mapping (Fig. 1d, e). Notably, such large agglomerates did not form in the absence of LiCl (Supplementary Fig. 6), indicating that lithiation triggers agglomeration.

Structure analyses confirmed that the agglomeration is coupled to Li intercalation. X-ray diffraction (XRD) peaks shifted clearly without losing their sharpness (Fig. 2a), indicative of intercalation while maintaining crystallinity. In contrast, such a shift was not observed and the peak intensity decreased when LiCl was omitted from PBS (Supplementary Fig. 7), indicating that a Li source is required to prevent reductive dissolution and/or amorphization under these conditions. X-ray absorption near-edge structure (XANES) analysis and inductively coupled plasma optical emission spectroscopy (ICP-OES) indicated Li intercalation to form $Li_{1-x}Mn_2O_4$ (Fig. 2b and Supplementary Fig. 8). Lactate was indispensable for MR-1 metabolism and lithiation; without lactate, neither process proceeded (Fig. 2c). Consistently, lactate-derived CO_2, negligible acetate production, and a slight decrease in pH correlated with the electrochemical capacity (Supplementary Fig. 9), in line with a bioelectrochemical reduction pathway. In contrast, abiotic chemical reduction of λ-MnO_2 by lactate could partially allow Li intercalation but cause a crystallinity loss (Supplementary Fig. 10). Importantly, acetate and other possible products (*i.e.*, pyruvate, formate, acetaldehyde) at observed concentration ranges could not explain the extent of bioelectrochemical Li intercalation (Supplementary Figs. 11–13), indicating negligible contributions of diffusible metabolic reductants. Furthermore, abiotic λ-MnO_2 reduction ceased within several hours (Supplementary Fig. 14), while biotic reaction

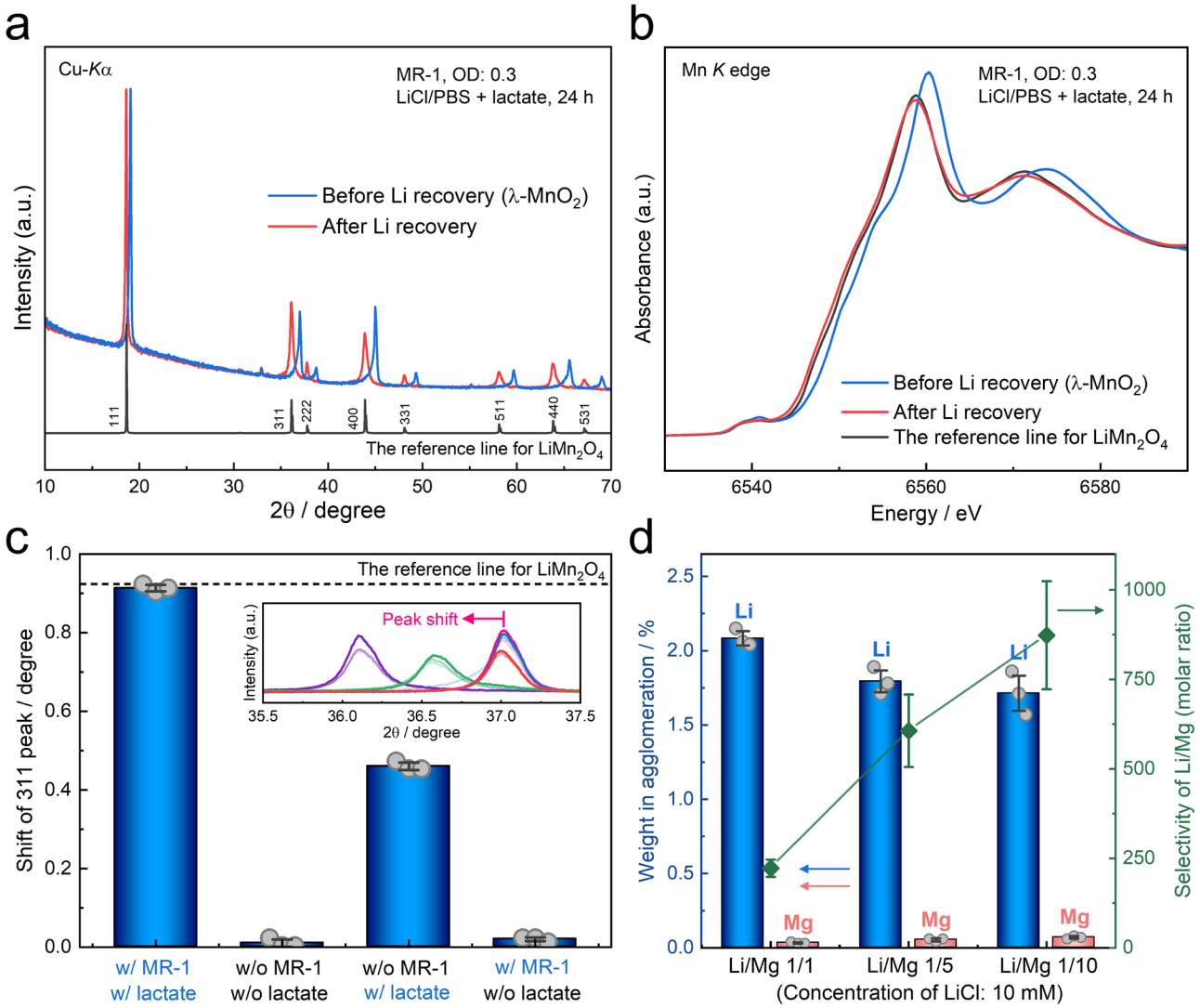


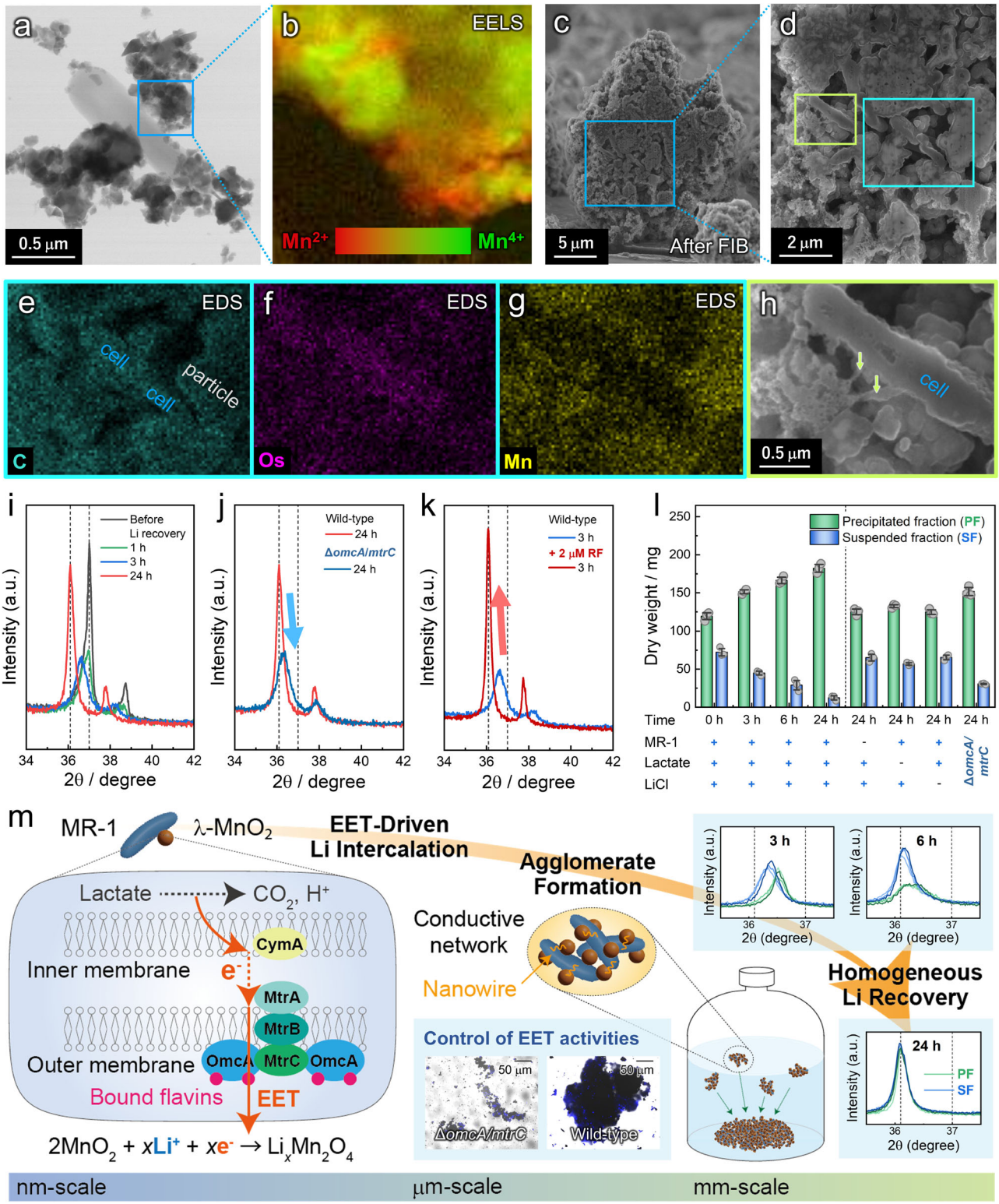
Fig. 2 | Bioelectrochemical Li intercalation into λ-MnO_2. **a** XRD patterns and (**b**) XANES spectra of the materials before and after bioelectrochemical Li recovery in LiCl/PBS and those of $LiMn_2O_4$ for reference. **c** Shift of the 311 peak in the XRD profiles under different conditions of MR-1 and lactate. The inset shows the corresponding XRD profiles [pink: before Li recovery (*i.e.*, λ-MnO_2); purple: w/ MR-1, w/ lactate; blue: w/o MR-1, w/o lactate; green: w/o MR-1, w/ lactate; red: w/ MR-1, w/o lactate], where w/ and w/o represent with and without, respectively. **d** Weight (left) and selectivity (right) of Li/Mg measured through ICP-OES for the agglomerate prepared in LiCl–$MgCl_2$/PBS solutions with different Li/Mg ratios. In c and d, data are presented as mean values ± standard deviation (s.d.), $n = 3$ independent biological replicates.

continuously proceeded until the end state. Given that the chemical lithiation formed an intermediate $Li_xMn_2O_4$ (x = ~0.5), the less energetically favourable reaction (x > ~0.5) is principally driven by microbial electron input. These results demonstrate that microbial metabolism accelerates Li intercalation beyond the chemically accessible intermediate states while preserving material integrity, establishing a distinct bioelectrochemical intercalation mechanism hardly achievable by purely chemical processes.

The selectivity of Li intercalation was further confirmed using Li–Mg mixed solutions. Although λ-MnO_2 prevents the intercalation of other alkali metals, this was not the case for Mg^{2+} because its ionic radius is similar to that of Li^+[35]. The molar ratio of Li/Mg was 200–1000 times more concentrated in the agglomerates compared to the solution (Fig. 2d). This is reasonable from the kinetic analysis, in that the order was consistent with the difference in diffusion distances estimated from their activation energies (Supplementary Fig. 15). Such slow kinetics of Mg^{2+} diffusion in spinel-oxide materials are well known in the field of Mg-ion batteries[36–38]. The intercalation of Na^+ and K^+ was negligible (Supplementary Table 2), even though they were abundant in PBS solutions. Furthermore, the XRD and XANES profiles of intermediate states prepared by limiting the amount of Li in the vials (Supplementary Figs. 16–19) were consistent with reported electrochemical charge/discharge of $LiMn_2O_4$/λ-MnO_2[5,39,40], although the Li depletion led to the above-mentioned crystallinity loss. Therefore, under Li-sufficient conditions, the Li intercalation behaviour exhibited by our bioelectrochemical approach closely resembles that observed in electrode-driven systems.

Cell–material interface and electron transfer

Direct electron transfer at the cell/particle interface, however, cannot fully explain the spatially homogeneous and efficient lithiation observed within the agglomerates, as a limited number of λ-MnO_2 particles directly contact MR-1 cells within the agglomerate (Fig. 1d, e). This suggests the formation of a long-distance electronic network in the agglomerate, comprising semiconductive nanoparticles wired by the extracellular or cell-surface cytochromes[28]. To analyse the cellular and material interface formed during agglomeration, we performed electron energy loss spectroscopy (EELS) mapping with



scanning transmission electron microscopy (STEM). Subsequent to agglomeration, the Li-containing aggregated material was dispersed by ultrasonication to prepare smaller pieces that could be mounted on a TEM grid. The nanoparticles attached to the cells exhibited no obvious changes in morphology (Fig. 3a), and Mn valency evaluated by EELS decreased from +4 (initial state) to typically around +3.5 (after Li intercalation) even if Mn was not directly attached to the cell (Fig. 3b), consistent with electron delivery beyond immediate cell–particle junctions. Mn was not detected inside the cell through EELS (Fig. 3b), STEM–EDS (Supplementary Fig. 20), or cross-sectional TEM (Supplementary Fig. 21), indicating that Mn-based nanoparticles did not originate from dissolved Mn ions reduced in the cells. Despite hardly detectable dissolved Mn in the supernatant or its bulky deposition, EELS and TEM results revealed the presence of a small amount of Mn^{2+} in the vicinity of the microbes (Supplementary Fig. 22). Since this impurity phase was undetectable by XRD, it is most consistent with an amorphous or nanocrystalline hydrated Mn phosphate[41].

Fig. 3 | EET-driven electrochemical reaction. a STEM and (**b**) EELS mapping images for a dispersed composite of MR-1 and nanoparticles after bioelectrochemical Li recovery. **c** SEM image after FIB milling of an agglomerate piece and (**d**) its enlarged view. **e**–**g** EDS mapping images of the cross-section, where Os suggests stained OM *c*-Cyts. **h** Enlarged view of the cross-section showing nanowire-like structure (pointed by arrows) along with a cell. Similar micrographic results were obtained in at least two independent experiments. XRD profiles after bioelectrochemical Li recovery from 10 mM LiCl/PBS at (**i**) different reaction times as well as those with (**j**) a mutant strain lacking OM *c*-Cyts (Δ*omcA/mtrC*) and with (**k**) 2 μM riboflavin (RF) for enhancing the rate of EET. The peak positions of $LiMn_2O_4$ and λ-MnO_2 are shown by dashed grey lines for comparison. The optical density of the MR-1 cell suspension was 0.3. **l** Dry weight of the precipitated fraction (PF) and suspended fraction (SF) during the Li recovery process with wild-type MR-1, where these fractions were prepared by resuspending the precipitate and then separating the bottom 20% (PF) and the top 80% (SF) after waiting for 1 min. Control experiments omitting either MR-1, lactate, or LiCl were carried out, in addition to the case using the mutant strain (Δ*omcA/mtrC*). Data are presented as mean values ± standard deviation (s.d.), $n = 3$ independent biological replicates. **m** Schematics showing the reaction scheme highlighting EET-driven Li intercalation, agglomerate formation, and homogeneous Li recovery. The left panel illustrates the direct EET mechanism from MR-1 to λ-MnO_2, where the electrons stemming from lactate are provided to OM *c*-Cyts while releasing CO_2 gas and protons. To further effectively reduce the material, bacteria and nanoparticles form agglomerates, likely with bacterial phenotype shift including nanowire formation. As confirmed by control experiments, such as using mutant strains, this agglomeration is linked to the activity of EET. These micron-scale fractions further grow to form a macroscopic precipitate at the bottom of the reactor during the Li recovery process, as illustrated in the right panel. The illustration was created using Adobe Illustrator.

Focused ion beam (FIB) milling with cross-sectional SEM–EDS was employed for the direct observation of the cellular morphology inside the agglomerates. Note that the agglomerate was subjected to 3,3′-diaminobenzidine (DAB)-H_2O_2 and OsO_4 staining in advance for labelling redox-active enzymes, including cytochromes[42]. We selected a small piece with a diameter of 10–20 μm (Supplementary Fig. 23) and subjected it to FIB milling to expose a cross-section (Fig. 3c, d). Os signals were localized near microbes but observed with Mn in the EDS mapping (Fig. 3e–g and Supplementary Fig. 24). Carbon incorporated in λ-MnO_2 was also detected through EDS; the results suggested the expression of the extracellular and cell-surface cytochromes to physically and electrically support the microbial/material composite. In addition, we observed a nanowire-like structure that facilitates electrical conduction via cytochromes[23], bridging microbes and nanoparticles (Fig. 3h), and suggesting a possible mechanism for electron transfer and agglomerate formation in this system[43].

EET controls Li intercalation

To investigate the critical role of the extracellular and cell-surface cytochromes in agglomeration-coupled Li recovery, we utilized a gene deletion mutant, specifically Δ*omcA/mtrC*, lacking key outer membrane cytochromes (OM *c*-Cyts), which mediate EET at the solid interface and facilitate long-range electron transfer via membrane vesicles or nanowires[23,44]. Unlike the wild-type strain, which showed significant λ-MnO_2 reduction to the end state (Fig. 3i), the Δ*omcA/mtrC* mutant exhibited incomplete reduction even after 24 h (Fig. 3j), confirming that full Li intercalation requires cellular machinery and is not a result of chemical mediation. Fluorescence microscopy of the Δ*omcA/mtrC* mutant revealed minimal agglomeration and cellular attachment to the surface of λ-MnO_2 (Supplementary Fig. 25), indicating that OM *c*-Cyts are key drivers of both EET and the initiation of the microbial–material interactions to agglomerate. Additionally, leveraging a mutant strain[45] lacking extracellular polysaccharide to facilitate OM *c*-Cyts making contact with λ-MnO_2 surface enhanced agglomeration with λ-MnO_2 and accelerated the rate of Li intercalation relative to the wild type (Supplementary Fig. 26).

To further confirm the role of OM *c*-Cyts in lithiation, we examined the effect of riboflavin, a known non-covalently bound semiquinone cofactor that enhances direct EET via OM *c*-Cyts[46,47]. The addition of 2 μM riboflavin accelerated Li intercalation kinetics by approximately eightfold (Fig. 3k). In contrast, riboflavin alone had a negative effect on abiotic λ-MnO_2 reduction by lactate (Supplementary Fig. 27), indicating that the enhancement requires the bacterial EET machinery. Furthermore, rate enhancement by riboflavin was observed in the Δ*mtrC* mutant but not in the Δ*omcA* mutant, demonstrating that bound flavin cofactors specifically accelerate direct EET to λ-MnO_2 via OmcA rather than MtrC (Supplementary Fig. 28). Increasing the riboflavin concentration up to 100 μM did not enhance the reaction rate (Supplementary Fig. 29), suggesting that indirect electron transport via soluble hydroquinone diffusion plays a negligible role under our conditions[48]. This conclusion was further supported by the absence of enhanced rate in the cell-free supernatant solution obtained from a microbial Li-recovery reactor or from dead cell fractions (Supplementary Fig. 30). These results establish that MR-1-driven lithiation proceeds predominantly via a direct EET mechanism involving OM *c*-Cyts. This direct mechanism eliminates the reliance on soluble mediators, whose limited diffusion and concentration often constrain scalability in large-scale processes, thereby reinforcing the practical viability of our bioelectrochemical approach.

Scale-up potential of self-assembled agglomerates

Time-resolved fractionation experiments further demonstrate that EET does more than supply charge; it nucleates a hierarchically organized solid network that drives process scalability. When the λ-MnO_2 nanoparticles and MR-1 cells were incubated under Li-recovery conditions, the dry-mass ratio of the suspended (SF) (< approximately 10 μm) to the precipitated (PF) fractions declined monotonically while total mass remained constant (Fig. 3l and Supplementary Fig. 31). This shift indicates a transition from dispersed to agglomerated states, rather than mass growth or loss. Concomitantly, $Li_{1-x}Mn_2O_4$ formed first in SF and later in PF (Fig. 3m, right), demonstrating that Li intercalation proceeds and then propagates agglomerate growth. Agglomeration was abolished in the control conditions—omitting LiCl or lactate (Supplementary Fig. 32), or deleting the MtrC and OmcA—confirming that EET-driven intercalation is indispensable for these steps (Fig. 3m, l). Consistently, lowering Li concentration suppressed agglomeration (Supplementary Figs. 33–35). Such EET-associated adhesion to solid electron acceptors, together with associated phenotypic shifts (including the formation of a long-distance electron transfer pathway), is widely observed in microbial–electrode systems under EET conditions[28,44]. Given that agglomeration concentrates cells and intercalation hosts into a densely packed microenvironment, we envisage that direct EET via the extracellular and cell surface MtrC/OmcA not only nucleates the self-agglomerates, but that the resulting architecture can in turn reinforce cellular charge delivery, thereby establishing a biologically mediated positive-feedback loop that further accelerates Li intercalation as the agglomerate grows.

At the materials level, because smaller particles lithiate faster (Supplementary Fig. 36), EET would initiate at the nanoscale domains, knitting them into 10–50 μm clusters whose XRD profiles converge to a well-crystallized phase irrespective of agglomerate size. This bottom-up self-assembly creates a three-dimensional, electronically percolated architecture that retains nanoparticles usually lost in conventional processes[49,50], thereby maximizing material utilization. The electronically conductive lithiated materials can further accelerate electron flow[51,52], establishing a materials-level positive feedback loop that sweeps dispersed particles into the growing network. Such self-assembled living composites circumvent the mass-loading limitations

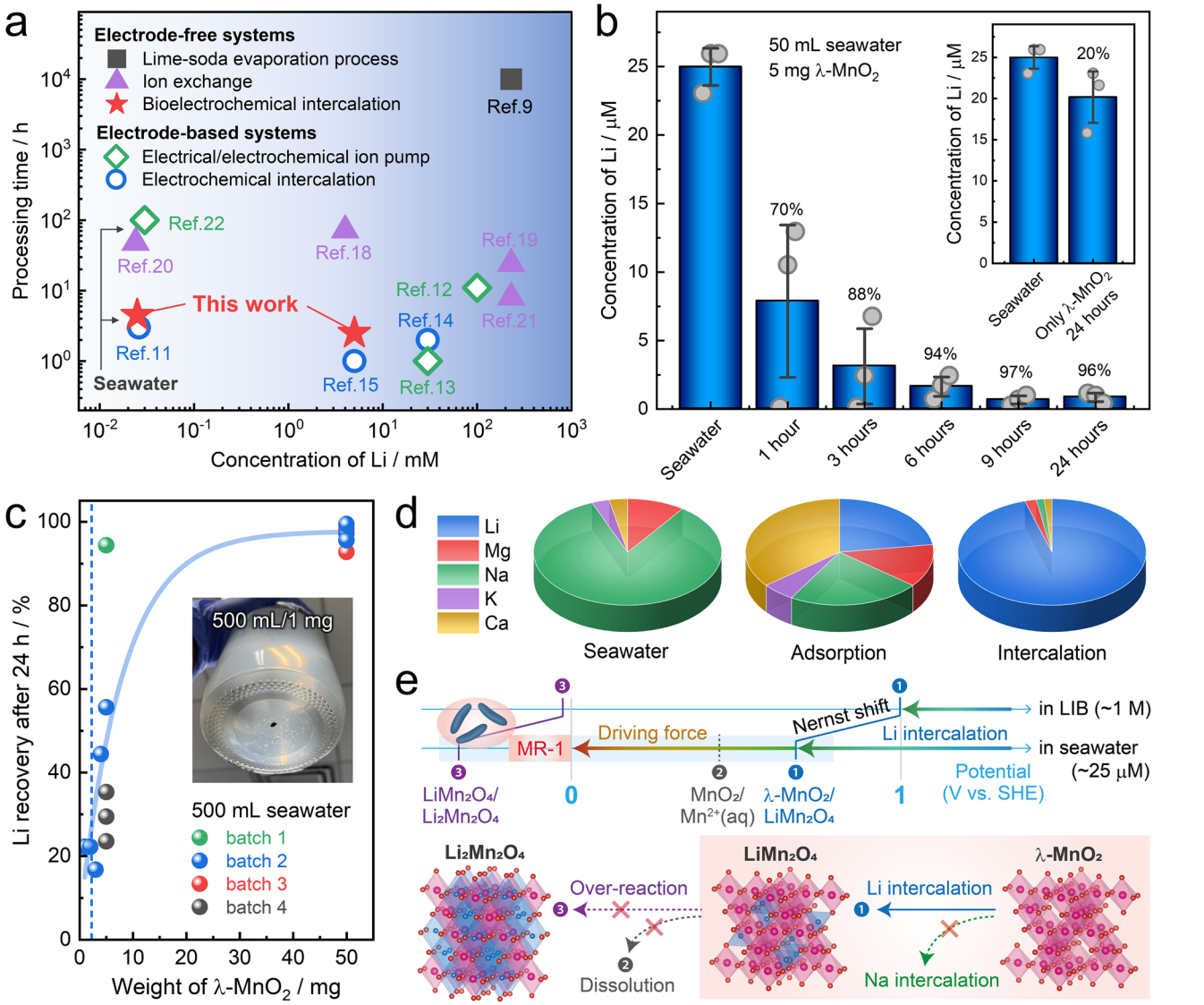


Fig. 4 | Li recovery from real seawater. a Li recovery performance of this study in seawater (left star) and PBS (right star) compared with selected previously reported systems. **b** Concentration of dissolved Li in real seawater before and after bioelectrochemical Li recovery at a seawater/λ-MnO_2 ratio of 50 mL/5 mg. The inset shows the case where only λ-MnO_2 was used without MR-1 and lactate. Each plot was from a different sampling batch of seawater. **c** Bioelectrochemical Li recovery performance after 24 h for 500 mL seawater depending on the amount of λ-MnO_2. Each plot was coloured by the batch of seawater experiments, and the blue curve is an exponential fit for batch 2, provided as a guide. The blue line indicates the theoretical amount of λ-MnO_2 for collecting all Li from 500 mL seawater. The inset shows agglomeration formed at the bottom of the reactor with a high seawater/λ-MnO_2 ratio of 500 mL/1 mg. In b and c, the optical density of the MR-1 cell suspension was 0.3. **d** Composition (mass ratio) of Li, Mg, Na, K, and Ca for seawater (left), adsorption (middle), and intercalation (right) into λ-MnO_2 during bioelectrochemical Li recovery. **e** Schematic diagram showing the reaction mechanisms during bioelectrochemical Li recovery in low-concentration Li sources such as seawater. The potential for Li intercalation shifts due to the Nernst equation by approximately 0.3 V from that in conventional LIBs; however, it is still higher than the typical reduction potential of MR-1 and the dissolution potential of MnO_2. Therefore, MR-1 is suitable for obtaining a large driving force for Li intercalation while preventing over-lithiation to form $Li_2Mn_2O_4$. Furthermore, Li intercalation proceeds within the electrochemical window of water at neutral pH, as indicated by the light blue shadow. The bottom panel summarizes the selective Li intercalation pathways during our bioelectrochemical process. The illustration was created using Adobe Illustrator. In b, data are presented as mean values ± standard deviation (s.d.), $n = 3$ independent biological replicates.

that constrain conventional electrodes[4–6], yet deliver comparable Li-recovery rates (Fig. 4a)[14,15]. By yielding a solid slurry instead of suspension, the process minimizes downstream water handling and heat input, providing a mechanistic basis for scalable, energy-efficient Li recovery.

Robust Li recovery from real seawater

To evaluate the broader applicability of our bioelectrochemical method across a wide range of Li concentrations, we next tested real seawater. Although dissolved Li in seawater (approximately 25 μM) is orders of magnitude more abundant than in most freshwater systems[11,22], its recovery remains technically demanding[2,53,54]. We incubated MR-1 cells and λ-MnO_2 nanoparticles (5 mg) in lactate-supplemented seawater (50 mL) under anaerobic conditions. As shown in Fig. 4b, Li was extracted from seawater within several hours, consistent with the PBS-based experiments without riboflavin. In natural seawater, Li removal in the absence of MR-1 was strongly batch dependent; in lactate-supplemented seawater without adding MR-1, Li recovery after 24 h varied from ~20% to ~80% across independent seawater samples (Supplementary Fig. 37). By contrast, inoculation

with MR-1 cells consistently yielded ~95% recovery under otherwise identical conditions and was accompanied by self-agglomeration, demonstrating that the bioelectrochemical pathway confers robustness against matrix-to-matrix variability in the environmental waters. Notably, despite the much lower Li concentration, we did not observe an obvious crystallinity loss under seawater conditions (Supplementary Fig. 38). This contrasts with phosphate-buffered, Li-depleted conditions, where reductive formation of phosphates occurs once Li becomes limiting. Consistently, λ-MnO_2 in seawater without any added reductant (*i.e.*, with neither lactate nor MR-1) removed only ~20% Li presumably via surface adsorption (inset in Fig. 4b).

Across the different seawater batches, we observed modest batch-to-batch variations in kinetics, especially before ~3 h (Fig. 4b), consistent with the expected compositional variability of environmental samples. Indeed, the Li recovery kinetics were enhanced approximately twofold by spiking 2 μM riboflavin (Supplementary Fig. 39), indicating that the EET-driven intercalation rate can be sensitively modulated by trace redox-active constituents. We further evaluated Li recovery performance at harsh conditions with higher volume and/or higher seawater/λ-MnO_2 ratios (Fig. 4c), where the self-agglomeration was observed even at a high ratio of 500 mL/1 mg (inset in Fig. 4c). The reproducible Li recovery rate against matrix-to-matrix variability was confirmed even for 500 mL seawater when the amount of λ-MnO_2 was 50 mg, while it varied at 5 mg or lower. This behaviour is consistent with a capacity-limited regime; the dashed blue line in Fig. 4c indicates the stoichiometric minimum λ-MnO_2 required to capture all the Li present in 500 mL seawater. Accordingly, the blue curve, an exponential fit for batch 2, shows a threshold near this theoretical limit. Even under a challenging condition of 500 mL/5 mg, the highest utilization of the theoretical host capacity reached 42.6%, while maintaining efficient Li recovery from seawater. Remarkably, our method achieved highly selective Li intercalation from seawater (Fig. 4d). This was evaluated by comparing the compositions between the materials soaked in seawater and after bioelectrochemical Li recovery (Supplementary Tables 3 and 4). In strong contrast to the non-selectively adsorbed cations, the molar ratios of Li/*M* (*M* = Na, Mg, K, Ca) electrochemically intercalated into the material were all greater than 100 (Supplementary Table 5).

Energetic basis and generality of bioelectrochemical intercalation

While the exceptional Li/*M* selectivity in seawater is ultimately rooted in the intrinsic ion-sieving lattice of λ-MnO_2, our advance is to preserve this selectivity at electrochemical rates[11], without using any external electrodes. Bacterial EET furnishes the redox potential normally supplied by a power source, allowing λ-MnO_2 to operate in a fully three-dimensional, self-assembled reactor. In contrast to MnO_2-based ion-exchange sorbents[22], the continuous bioelectrochemical driving force accelerates ion insertion by an order of magnitude, uniting high discrimination with process kinetics previously accessible only to wired electrode systems. Li intercalation into λ-MnO_2 to form $LiMn_2O_4$ occurs at around 4 V vs. Li^+/Li (approximately 1 V vs. SHE) in concentrated Li solutions like LIB electrolytes[55], whereas the equilibrium potential drops by about 0.3 V in seawater due to its low Li concentration (Fig. 4e). Nevertheless, it is still higher than the potentials of typical MnO_2 dissolution[56] and the microbial reduction[46], providing a strong driving force for Li intercalation while preventing undesired transformation into over-lithiated $Li_2Mn_2O_4$[55]. These energetic considerations are consistent with the observed microbial–material coupling (Fig. 3m). The same concept is further supported by Li intercalation into an $FePO_4$ scaffold (Supplementary Fig. 40), which shows negligible abiotic reactivity under PBS conditions and therefore provides an orthogonal test of the bioelectrochemical driving principle. In addition, alternative electron donors, such as formate, also supported the microbial metabolism coupled to Li intercalation (Supplementary Fig. 41), expanding the choice of electron donors. Together, these results provide a foundation for future optimization strategies, such as pre-treatment of Li sources[57] or structural modification of λ-MnO_2[17,38], to further enhance Li intercalation efficiency and overall system performance.

Techno-economic and life-cycle assessments

Finally, we conducted comprehensive techno-economic analysis (TEA) and life-cycle assessment (LCA) to evaluate the prospective process boundary and feasibility of this approach under the assumed configuration. Considering that electrogenic bacterial strains capable of reducing MnO_2 under brine-level salinity conditions have been isolated[58], we used data from LiCl/PBS solution experiments to estimate the potential for Li_2CO_3 production from brine sources. In the assumed flow sheet (Supplementary Figs 42 and 43), the process relies on slurry recovery through settling/clarification and dewatering rather than membranes, and the material-clarified brine is subsequently treated in a brine-compatible polishing train before reinjection; these unit operations are included in the TEA/LCA. The following Li recovery process involved oxidizing $Li_{1-x}Mn_2O_4$ with $Na_2S_2O_8$ to obtain a Li-containing solution while regenerating λ-MnO_2 (Supplementary Fig. 44)[57,59], with only a 0.001% Mn loss (Supplementary Fig. 45). Residual bacteria were removed by heating to 90 °C (Supplementary Fig. 46) and further sterilized with $Na_2S_2O_8$, ensuring that subsequent steps are entirely abiotic. The regenerated λ-MnO_2 exhibited low byproduct formation and high structural reversibility (Supplementary Figs. 47 and 48).

The Li-containing solution underwent Mn-ion removal, volume reduction, and Li_2CO_3 precipitation with the addition of Na_2CO_3, resulting in an industrial-grade purity of ~98% (Supplementary Fig. 49). Biomass contamination in the delithiated solution was below the detection limit based on biochemical oxygen demand tests. To protect environmental integrity, the spent brine containing bacteria and lactate is treated via a brine-compatible polishing train, where they are removed in the aeration tank, clarifier, chlorination, gravity thickening and belt pressing, ensuring safe reinjection with minimal water loss (see Supplementary Note 1 for costing assumptions). Under this assumed configuration, the estimated production cost of Li_2CO_3 using our method is 6.06 USD/kg (Supplementary Fig. 42b), comparable to the commercial direct lithium extraction (DLE) utilizing Li–Al double-layer hydroxides[60] as well as the conventional evaporation methods for brine sources[61–63], and remains below the current market price for similar grade Li_2CO_3 (Supplementary Table 6). Additionally, our LCA indicated a low water footprint of 0.44 m^3eq/kg Li_2CO_3 (Supplementary Fig. 42c) with minimal brine water loss, significantly outperforming conventional methods[60,63], highlighting the potential of our technology to alleviate local water conflicts[3,9,10]. The estimated climate change impact, 16.99 kg CO_2eq/kg Li_2CO_3 (Supplementary Fig. 42d), was moderately higher than the conventional evaporation methods in Atacama and Olaroz brines[63], primarily due to the use of $Na_2S_2O_8$ (Supplementary Fig. 50). Developing alternative, greener oxidants is therefore a key avenue for further sustainability improvements. Crucially, continuous solid/liquid separation for microbial products already sustains approximately 5000 tons per year throughput[64,65], underscoring that biotechnological unit operations analogous to our scheme can be scaled seamlessly to the tonnages demanded for commercial brine processing.

Our process concentrates Li as a recoverable $Li_xMn_2O_4$ slurry, conferring decisive advantages over both evaporation and adsorption-based DLE routes. Because the product is removed as a solid rather than by bulk-phase boiling, brine water loss is minimal, eliminating the vast evaporative footprint of solar ponds. Unlike sorbent systems, our slurry-based recovery could reduce the need for heated strip solutions, thereby avoiding the major energy penalty of Li concentration[60]. The λ-MnO_2 host further surpasses the Li–Al double-layer hydroxides in

recyclability and intrinsic Li selectivity, while the microbially driven bottom-up self-assembly recovers even nanoscale particles that conventional adsorbents discard[49,50], minimizing material consumption and raw-material cost. Moreover, cation substitution in the λ-MnO_2 framework can further stabilize the lattice while preserving the performance[17], offering an additional route to enhance both durability and process economics. In our present TEA/LCA, overall cost and impact are dominated by reagent and heat inputs; reaction rate plays a minor role. Under more kinetically challenging conditions[54]—for example, ultra-dilute brines—the intrinsically fast, electrochemical-rate Li recovery in our method would widen the performance gap over sorption or evaporation routes, making the advantages reported here a conservative estimate.

Discussion

In this study, we have demonstrated a scalable bioelectrochemical method for Li recovery, where *S. oneidensis* MR-1 bacteria autonomously agglomerate with λ-MnO_2 and $FePO_4$, facilitating direct EET and driving Li intercalation with efficacy and selectivity comparable to conventional electrode-based systems. Unlike these methods that are limited by the surface area of electrodes, our bioelectrochemical approach leverages self-organized agglomeration in a homogeneous system, enabling scalability without the need for electrodes with low cost and environmental impact. Although lactate mainly served as the electron donor in this study, this method could also be coupled to microbial metabolic anoxic oxidation of biomass[25], offering a low-carbon alternative for large-scale Li recovery[4,10]. As electron-donating bacteria flourish under various pH and salinity conditions[24,58], our approach has broad applicability for diverse Li recovery and recycling scenarios[66]. Future research should focus on improving the economic and environmental costs associated with oxidants used in Li leaching. For instance, the ability of dissimilatory metal-reducing bacteria to both donate and extract electrons from solids[67–69] suggests the possibility of combining microbial Li recovery with biomass-based oxidants and microbial electron uptake to further enhance sustainability. Exploring how Li intercalation activates this bacterial phenotype could provide critical insights for future microbial/material interface design. Ultimately, bioelectrochemical intercalation offers a versatile strategy for Li recovery and may enable broader applications in the handling of alkali and alkaline-earth metals under ambient conditions, as well as advancing materials synthesis, such as electrochemical tuning of intercalation materials for energy and environmental technologies[70].

Methods

Synthesis

λ-MnO_2 was prepared from $LiMn_2O_4$ using an acid-leaching process[71]. $LiMn_2O_4$ particles (0.3 g) were placed in a glass bottle, filled with 0.4 M HCl aqueous solution (30 mL), and stirred for 24 h at room temperature. The obtained material was filtered and washed several times with pure water, followed by vacuum drying for 10 h at 100 °C. The synthesised λ-MnO_2 powder was stored in a desiccator until used in Li recovery experiments. $LiMn_2O_4$ was synthesised using a solution combustion method[72,73], as briefly described below: $LiNO_3$ (Wako Chemicals, 98%), $Mn(NO_3)_2{\cdot}6H_2O$ (Wako Chemicals, 98%), and citric acid (Wako Chemicals, 98%) were dissolved in water. The temperature of the solution was carefully increased to evaporate the liquid until a gel was formed. Subsequently, the gel was ignited by a sudden increase in temperature. Heat treatment was carried out for 4 h at 700 °C in an air atmosphere to increase the crystallinity and decrease the impurity phase. Carbon-coated $LiFePO_4$ (Hohsen Corporation, battery grade) was subjected to $K_2S_2O_8$ (Sigma-Aldrich, 99%) to prepare $FePO_4$[74]. Typically, 11.7 g of $LiFePO_4$ was stirred at room temperature for 24 h in the solution with 370 mL of pure water and 10 g of $K_2S_2O_8$. The delithiated material was collected by filter paper, washed with pure water, and vacuum-dried for 18 h at 80 °C. All materials were stored in a desiccator before use. VESTA[75] was used to visualise the crystal structures of the oxides and the Li diffusion paths.

Bacterial preparation

Shewanella oneidensis. MR-1 was purchased from ATCC (700550D) and the strain was stored in a deep freezer (−80 °C) before plating on agar plates. The deletion mutant strains were kindly provided by Prof. Kenneth Nealson (University of Southern California) or Prof. Atsushi Kouzuma (Toyo University). The wild-type *Shewanella oneidensis* MR-1 and the mutant strains lacking OmcA and/or MtrC (Δ*omcA/mtrC*, Δ*omcA*, Δ*mtrC*) and the cell surface polysaccharides (ΔSO3177) were grown aerobically in a Luria-Bertani (LB) medium (10 g/L tryptone, 5 g/L yeast extract, and 10 g/L NaCl) at 30 °C overnight. Then, the culture was centrifuged for 10 min, and the LB medium was replaced with PBS (8 g/L NaCl, 0.2 g/L KCl, 0.24 g/L KH_2PO_4, and 1.44 g/L Na_2HPO_4; pH 7.4). After removing the LB medium, the concentration of bacteria was adjusted to the given optical density (OD), typically 0.3, at 600 nm before use in Li recovery experiments.

Bioelectrochemical Li recovery

PBS-based LiCl solutions and real seawater were used for the Li recovery experiments. LiCl (Wako Chemicals, 99%) and lactate (Wako Chemicals, sodium L-lactate solution, 70%) were dissolved in PBS and left overnight to obtain homogeneous solutions. $MgCl_2$ (Wako Chemicals, 97%) was also dissolved to examine the performance in the Li–Mg mixed solutions. Sodium acetate (Wako Chemicals, 98.5%), pyruvate (Nacalai Tesque, 97%), formate (Wako Chemicals, 98%), and acetaldehyde (Wako Chemicals, 90%) were used for electron donors in control experiments. Seawater samples were taken from Oarai in Ibaraki, which is on the east side of Japan. Unless otherwise noted, Oarai seawater with 50 mM lactate was used for Li recovery experiments. The seawater was passed through 0.2 μm sterile filters to remove contaminated cells prior to use.

The Li-containing solution and λ-MnO_2 nanoparticles were placed in a glass bottle, and dissolved oxygen was eliminated by N_2 bubbling. The typical amount of λ-MnO_2 used for the experiments with 50 mL PBS solution was 50 mg. Subsequently, microbes were injected into the reactor, and the mixture was shaken at 30 °C in an incubator. The obtained agglomerates could be easily separated from the supernatant liquid because they were attached to the bottom of the reactor, as seen in Fig. 1a. The agglomerates were dispersed in pure water by ultrasonication and were washed by treatment with 2% Triton X-100 (Sigma-Aldrich) for 15 min. The process of centrifugation and replacement with pure water was repeated five times to purify the material. Regarding the $FePO_4$ experiment, the washing process was performed in a glove box to suppress the reoxidation of Li-intercalated material. Vacuum drying at 100 °C for 18 h was performed to completely remove the water. The Li concentrations before and after Li recovery were analysed through ICP-MS/OES at the Materials Analysis Station, NIMS, and at the Analytical Research Core for Advanced Materials, Institute for Materials Research, Tohoku University. CO_2 gas generated from lactate metabolism was measured by a gas chromatography-mass spectrometry (Agilent 7000D) coupled with a HP-PLOT/Q column (30 m length, 0.32 mm diameter, and 20 μm film thickness). For the time-course experiments, the precipitate was resuspended and stood for 1 min, and then the 80% from the top and the remaining 20% were assigned to the suspended and precipitated fractions, respectively.

Characterisation

XRD with Cu-*K*α was performed using an X-ray diffractometer (Rigaku, SmartLab) at the NIMS Battery Research Platform. Rietveld analysis was carried out using the RIETAN-FP programme[76] to evaluate the lattice constant. The particle size of the synthesised material was evaluated using a nanoparticle tracking analyser (Particle Metrix, ZetaView), where the sample was prepared by ultrasonication to

disperse λ-MnO_2 nanoparticles in pure water. SEM–EDS (JEOL, JSM-7800F) of the agglomerate of bacteria and nanoparticles was performed at the NIMS Battery Research Platform after a dehydration process. Briefly, the material was immersed in 10% glutaraldehyde overnight, and the supernatant liquid was gradually changed to higher concentrations of ethanol. 100% ethanol was then replaced with tert-butyl alcohol, and the material was freeze-dried overnight, followed by Pt coating to increase conductivity.

Bright-field and fluorescence images were obtained using an inverted microscope (Leica DMi8, Leica) combined with a microcamera (Leica, Leica DFC9000). An agglomerate in the culture vial, after decanting to remove the supernatant, was resuspended by pipetting with 5 mL of pure water, where the pure water (18.2 MΩ cm) used for this work was purified with a Direct-Q 5 UV system (Millipore). To obtain fluorescence microscopy images of DNA-stained MR-1 cells, 2 μL of the resuspended agglomerate was mixed with 2 μL of 4′,6-diamidino-2-phenylindole (DAPI, 0.5 μg/mL) on a microscope slide, and it was kept in the dark at 4 °C for 3 min before microscopy. A DAPI filter was used to obtain fluorescence microscopy images.

XANES spectra were obtained at BL-12C, Photon Factory, Japan, where boron nitride (Mitsuwa Chemicals, 99.5%) was used to dilute the materials for XANES analysis. STEM–EELS (JEOL, JEM-ARM200F) for a microbial/material composite was conducted at the NIMS Battery Research Platform. The original sample was the same as that used for SEM–EDS, but it was dispersed in ethanol to be loaded onto a TEM grid. The EELS mapping showing the valence state of Mn was obtained by fitting the profile at each point with those of MnO (Mn^{2+}) and MnO_2 (Mn^{4+}) as the reference materials. Cross-sections of the agglomerates were characterised by FIB–SEM–EDS (Hitachi, SMF2000), where they were subjected to DAB-H_2O_2 and OsO_4 staining before the analysis. Cross-sectional TEM (JEOL, JEM-1400Plus) was performed using Tokai Electron Microscopy (Nagoya, Japan) for a resin-embedded sample sectioned with an ultramicrotome (Leica, Ultracut UCT).

Concentrations of metabolites were analysed by using an ion chromatography system (Shimadzu) equipped with an autosampler (SIL-10Ai), a liquid chromatograph pump (LC-20AD), a degassing unit (DGU-20A 3R), a column oven (CTO-20AC), a conductivity detector (CDD-10A VP), and a communication bus module (CBM-20A). The samples were diluted 100-fold by pure water, and the separation was performed on a non-suppressor column (Shim-pack IC-A3). Standard lines were obtained using a series of organic acid standards, which were prepared in pure water with and without $MnCl_2$ (Wako Chemicals, 99%). The injection volume for all samples and standards was 10 μL.

Techno-economic and life-cycle analyses

The environmental performance of our bioelectrochemical Li recovery method was evaluated based on the cradle-to-gate LCA of battery-grade Li_2CO_3[77] for ease of comparison with current manufacturing[63,78]. LCA was performed in openLCA v2.0 with the ecoinvent v3.10 database and the ReCiPe 2016 impact assessment method. An extended Li_2CO_3 precipitation was included based on our experiments described in the main text and Supporting Information. The Li extraction site was modelled on Salar de Atacama[63]. Within the system, λ-MnO_2 and water used for washing and Li concentration were assumed to be recyclable. The life cycle inventory was detailed in Supplementary Tables 7–15.

We modelled water consumption and climate change impact to represent the environmental performance of the technology. The background inventory, e.g., environmental loads of general chemical production and electricity generation, was adopted from ecoinvent 3.10, a commercial LCA database. The water consumption was categorized into in-situ water, brine water, and ex-situ water, to distinguish water stress with geography consideration. The climate change impact was characterized by the greenhouse gases' global warming potential over 100 years[79]; the contribution was breakdown into Li intercalation or concentration and Li_2CO_3 precipitation, to differentiate the contribution of this study.

TEA was conducted based on the same modelled system as the LCA, which assumed a factory producing 70,000-ton Li_2CO_3 per year and operating throughout the year (Supplementary Table 16). The cost of Li_2CO_3 production was calculated based on the annual operation expenditures, including raw materials, utilities, operation and maintenance, overhead, tax and insurance, general expenses, and asset depreciation. The prices of raw materials were obtained from online wholesale markets in China and the utility cost was based on the Chilean electricity rate, where the references are listed in Supplementary Table 17. We estimated the remaining operation and maintenace cost and the capital expenditures, represented as asset depreciation, based on an up-flow anaerobic sludge blanket (UASB) facility[80]. The UASB facility was assumed to resemble the Li intercalation facility designed in this study.

Statistics and reproducibility

For the LCA/TEA: no statistical method was used to predetermine sample size; no data were excluded; randomization and blinding are not applicable to this computational assessment. For bioelectrochemical observations, similar results were obtained in at least two independent experiments.

Reporting summary

Further information on research design is available in the Nature Portfolio Reporting Summary linked to this article.

Data availability

Data that support the findings of this study are available within the paper and the Supplementary Figs. and Tables. Background inventory data for LCA are from the ecoinvent v3.10 database and cannot be redistributed under the ecoinvent licence; these datasets are available to licensed users from ecoinvent (https://ecoinvent.org). The numerical data underlying the figures are provided as a Source Data file. Source data are provided with this paper.

References

1. Harper, G. et al. Recycling lithium-ion batteries from electric vehicles. *Nature* **575**, 75–86 (2019).
2. Swain, B. Recovery and recycling of lithium: a review. *Sep. Purif. Technol.* **172**, 388–403 (2017).
3. Vera, M. L., Torres, W. R., Galli, C. I., Chagnes, A. & Flexer, V. Environmental impact of direct lithium extraction from brines. *Nat. Rev. Earth Environ.* **4**, 149–165 (2023).
4. Calvo, E. J. Direct lithium recovery from aqueous electrolytes with electrochemical ion pumping and lithium intercalation. *ACS Omega* **6**, 35213–35220 (2021).
5. Kim, S., Kang, J. S., Joo, H., Sung, Y.-E. & Yoon, J. Understanding the behaviors of λ-MnO_2 in electrochemical lithium recovery: Key limiting factors and a route to the enhanced performance. *Environ. Sci. Technol.* **54**, 9044–9051 (2020).
6. Romero, V. C. E., Putrino, D. S., Tagliazucchi, M., Flexer, V. & Calvo, E. J. Electrochemical flow reactor for selective extraction of lithium chloride from natural brines. *J. Electrochem. Soc.* **167**, 120522 (2020).
7. Tarascon, J.-M. & Armand, M. Issues and challenges facing rechargeable lithium batteries. *Nature* **414**, 359–367 (2001).
8. Goodenough, J. B. & Park, K.-S. The Li-ion rechargeable battery: A perspective. *J. Am. Chem. Soc.* **135**, 1167–1176 (2013).
9. Battistel, A., Palagonia, M. S., Brogioli, D., La Mantia, F. & Trocoli, R. Electrochemical methods for lithium recovery: a comprehensive and critical review. *Adv. Mater.* **32**, 1905440 (2020).
10. Grosjean, C., Miranda, P. H., Perrin, M. & Poggi, P. Assessment of world lithium resources and consequences of their geographic

distribution on the expected development of the electric vehicle industry. *Renew. Sustain. Energy Rev.* **16**, 1735–1744 (2012).
11. Liu, C. et al. Lithium extraction from seawater through pulsed electrochemical intercalation. *Joule* **4**, 1459–1469 (2020).
12. Trocoli, R., Erinmwingbovo, C. & La Mantia, F. Optimized lithium recovery from brines by using an electrochemical ion-pumping process based on λ-MnO_2 and nickel hexacyanoferrate. *ChemElectroChem* **4**, 143–149 (2017).
13. Lee, J., Yu, S.-H., Kim, C., Sung, Y.-E. & Yoon, J. Highly selective lithium recovery from brine using a λ-MnO_2–Ag battery. *Phys. Chem. Chem. Phys.* **15**, 7690–7695 (2013).
14. Xu, X. et al. A self-supported λ-MnO_2 film electrode used for electrochemical lithium recovery from brines. *ChemPlusChem* **83**, 521–528 (2018).
15. Wang, L. et al. Electrochemical lithium recovery with lithium iron phosphate: What causes performance degradation and how can we improve the stability? *Sustain. Energy Fuels* **5**, 3124–3133 (2021).
16. Lawagon, C. P. et al. $Li_{1-x}Ni_{0.33}Co_{1/3}Mn_{1/3}O_2$/Ag for electrochemical lithium recovery from brine. *Chem. Eng. J.* **348**, 1000–1011 (2018).
17. Lawagon, C. P. et al. $Li_{1-x}Ni_{0.5}Mn_{1.5}O_4$/Ag for electrochemical lithium recovery from brine and its optimized performance via response surface methodology. *Sep. Purif. Technol.* **212**, 416–426 (2019).
18. Hong, H.-J. et al. Highly porous and surface-expanded spinel hydrogen manganese oxide (HMO)/Al_2O_3 composite for effective lithium (Li) recovery from seawater. *Chem. Eng. J.* **337**, 455–461 (2018).
19. Chitrakar, R., Makita, Y., Ooi, K. & Sonoda, A. Lithium recovery from salt lake brine by H_2TiO_3. *Dalton Trans.* **43**, 8933–8939 (2014).
20. Chitrakar, R., Kanoh, H., Miyai, Y. & Ooi, K. Recovery of lithium from seawater using manganese oxide adsorbent ($H_{1.6}Mn_{1.6}O_4$) derived from $Li_{1.6}Mn_{1.6}O_4$. *Ind. Eng. Chem. Res.* **40**, 2054–2058 (2001).
21. Chitrakar, R., Makita, Y., Ooi, K. & Sonoda, A. Selective uptake of lithium ion from brine by $H_{1.33}Mn_{1.67}O_4$ and $H_{1.6}Mn_{1.6}O_4$. *Chem. Lett.* **41**, 1647–1649 (2012).
22. Li, Z. et al. Continuous electrical pumping membrane process for seawater lithium mining. *Energy Environ. Sci.* **14**, 3152–3159 (2021).
23. Shi, L. et al. Extracellular electron transfer mechanisms between microorganisms and minerals. *Nat. Rev. Microbiol.* **14**, 651–662 (2016).
24. Garber, A. I. et al. FeGenie: a comprehensive tool for the identification of iron genes and iron gene neighborhoods in genome and metagenome assemblies. *Front. Microbiol.* **11**, 37 (2020).
25. Moradian, J. M., Fang, Z. & Yong, Y. -C.: Recent advances on biomass-fueled microbial fuel cell. *Bioresour. Bioprocess.* **8**, 14 (2021).
26. Deng, X., Luo, D. & Okamoto, A. Defined and unknown roles of conductive nanoparticles for the enhancement of microbial current generation: a review. *Bioresour. Technol.* **350**, 126844 (2022).
27. Myers, C. R. & Nealson, K. H. Bacterial manganese reduction and growth with manganese oxide as the sole electron acceptor. *Science* **240**, 1319–1321 (1988).
28. Nakamura, R., Kai, F., Okamoto, A., Newton, G. J. & Hashimoto, K. Self-constructed electrically conductive bacterial networks. *Angew. Chem.* **121**, 516–519 (2009).
29. Lloyd, J. R. Microbial reduction of metals and radionuclides. *FEMS Microbiol. Rev.* **27**, 411–425 (2003).
30. Belchik, S. M. et al. Extracellular reduction of hexavalent chromium by cytochromes MtrC and OmcA of *Shewanella oneidensis* MR-1. *Appl. Environ. Microbiol.* **77**, 4035–4041 (2011).
31. Springthorpe, S. K., Dundas, C. M. & Keitz, B. K. Microbial reduction of metal-organic frameworks enables synergistic chromium removal. *Nat. Commun.* **10**, 1–11 (2019).
32. Lovley, D. R. & Phillips, E. J. Novel mode of microbial energy metabolism: organic carbon oxidation coupled to dissimilatory reduction of iron or manganese. *Appl. Environ. Microbiol.* **54**, 1472–1480 (1988).
33. Leu, A. O. et al. Anaerobic methane oxidation coupled to manganese reduction by members of the *Methanoperedenaceae*. *ISME J.* **14**, 1030–1041 (2020).
34. Kitchaev, D. A., Dacek, S. T., Sun, W. & Ceder, G. Thermodynamics of phase selection in MnO_2 framework structures through alkali intercalation and hydration. *J. Am. Chem. Soc.* **139**, 2672–2681 (2017).
35. Shannon, R. D. Revised effective ionic radii and systematic studies of interatomic distances in halides and chalcogenides. *Acta Crystallogr. Sect. A Cryst. Phys. Diffr. Theor. Gen. Crystallogr.* **32**, 751–767 (1976).
36. Okamoto, S. et al. Intercalation and push-out process with spinel-to-rocksalt transition on Mg insertion into spinel oxides in magnesium batteries. *Adv. Sci.* **2**, 1500072 (2015).
37. Kim, C. et al. Direct observation of reversible magnesium ion intercalation into a spinel oxide host. *Adv. Mater.* **27**, 3377–3384 (2015).
38. Shimokawa, K. et al. Structure design of long-life spinel-oxide cathode materials for magnesium rechargeable batteries. *Adv. Mater.* **33**, 2007539 (2021).
39. Kanamura, K., Naito, H., Yao, T. & Takehara, Z. Structural change of the $LiMn_2O_4$ spinel structure induced by extraction of lithium. *J. Mater. Chem.* **6**, 33–36 (1996).
40. Shiraishi, Y., Nakai, I., Tsubata, T., Himeda, T. & Nishikawa, F. In situ transmission X-ray absorption fine structure analysis of the charge–discharge process in $LiMn_2O_4$, a rechargeable lithium battery material. *J. Solid State Chem.* **133**, 587–590 (1997).
41. Jin, K. et al. Hydrated manganese(II) phosphate ($Mn_3(PO_4)_2{\cdot}3H_2O$) as a water oxidation catalyst. *J. Am. Chem. Soc.* **136**, 7435–7443 (2014).
42. Deng, X., Dohmae, N., Nealson, K. H., Hashimoto, K. & Okamoto, A. Multi-heme cytochromes provide a pathway for survival in energy-limited environments. *Sci. Adv.* **4**, eaao5682 (2018).
43. Nakamura, R., Kai, F., Okamoto, A. & Hashimoto, K. Mechanisms of long-distance extracellular electron transfer of metal-reducing bacteria mediated by nanocolloidal semiconductive iron oxides. *J. Mater. Chem. A* **1**, 5148–5157 (2013).
44. Pirbadian, S. et al. *Shewanella oneidensis* MR-1 nanowires are outer membrane and periplasmic extensions of the extracellular electron transport components. *Proc. Natl. Acad. Sci.* **111**, 12883–12888 (2014).
45. Kouzuma, A., Meng, X.-Y., Kimura, N., Hashimoto, K. & Watanabe, K. Disruption of the putative cell surface polysaccharide biosynthesis gene SO3177 in *Shewanella oneidensis* MR-1 enhances adhesion to electrodes and current generation in microbial fuel cells. *Appl. Environ. Microbiol.* **76**, 4151–4157 (2010).
46. Okamoto, A., Hashimoto, K., Nealson, K. H. & Nakamura, R. Rate enhancement of bacterial extracellular electron transport involves bound flavin semiquinones. *Proc. Natl. Acad. Sci.* **110**, 7856–7861 (2013).
47. Xu, S., Jangir, Y. & El-Naggar, Y. M. Disentangling the roles of free and cytochrome-bound flavins in extracellular electron transport from *Shewanella oneidensis* MR-1. *Electrochim. Acta* **198**, 49–55 (2016).
48. Marsili, E. et al. *Shewanella* secretes flavins that mediate extracellular electron transfer. *Proc. Natl. Acad. Sci.* **105**, 3968–3973 (2008).
49. Su, J. et al. Continuous flow extraction of lithium from brine using silica-coated LMO beads. *Mater. Adv.* **6**, 2202–2210 (2025).
50. Disu, B. et al. Review of recent advances in lithium extraction from subsurface brines. *Geoenergy Sci. Eng.* **241**, 213189 (2024).
51. Kalantarian, M. M., Asgari, S. & Mustarelli, P. A theoretical approach to evaluate the rate capability of Li-ion battery cathode materials. *J. Mater. Chem. A* **2**, 107–115 (2014).

52. Li, J. et al. First-principles study of the effect of Ni-doped on the spinel-type Mn-based cathode discharge. *ACS Appl. Mater. Interfaces* **15**, 8208–8216 (2023).
53. Chen, X. et al. Spatially separated crystallization for selective lithium extraction from saline water. *Nat. Water* **1**, 808–817 (2023).
54. Yang, S., Wang, Y., Pan, H., He, P. & Zhou, H. Lithium extraction from low-quality brines. *Nature* **636**, 309–321 (2024).
55. Thackeray, M. M. Manganese oxides for lithium batteries. *Prog. Solid State Chem.* **25**, 1–71 (1997).
56. Sun, W., Kitchaev, D. A., Kramer, D. & Ceder, G. Non-equilibrium crystallization pathways of manganese oxides in aqueous solution. *Nat. Commun.* **10**, 573 (2019).
57. Pérez-Rodríguez, S., Fitch, S. D., Bartlett, P. N. & Garcia-Araez, N. $LiFePO_4$ battery material for the production of lithium from brines: effect of brine composition and benefits of dilution. *ChemSusChem* **15**, e202102182 (2022).
58. Yadav, S. et al. *Geoalkalibacter halelectricus* SAP-1 sp. nov. possessing extracellular electron transfer and mineral-reducing capabilities from a haloalkaline environment. *Environ. Microbiol.* **24**, 5066–5081 (2022).
59. Ooi, K., Miyai, Y., Katoh, S., Maeda, H. & Abe, M. Lithium-ion insertion/extraction reaction with λ-MnO_2 in the aqueous phase. *Chem. Lett.* **17**, 989 (1988).
60. Nikfar, S., Fahimi, A. & Vahidi, E. Unlocking sustainable lithium: a comparative life cycle assessment of innovative extraction methods from brine. *Resour. Conserv. Recycl.* **212**, 107977 (2025).
61. WSP Ambiental S.A. Technical report summary, operation report, Salar de Atacama. WSP-SQM0011-TRS-Salar-Rev1 (Sociedad Química y Minera de Chile S. A., 2022).
62. Huang, T.-Y., Pérez-Cardona, J. R., Zhao, F., Sutherland, J. W. & Paranthaman, M. P. Life cycle assessment and techno-economic assessment of lithium recovery from geothermal brine. *ACS Sustain. Chem. Eng.* **9**, 6551–6560 (2021).
63. Schenker, V., Oberschelp, C. & Pfister, S. Regionalized life cycle assessment of present and future lithium production for Li-ion batteries. *Resour. Conserv. Recycl.* **187**, 106611 (2022).
64. Amasawa, E., Yamanishi, T., Nakatani, J., Hirao, M. & Sato, S. Climate change implications of bio-based and marine-biodegradable plastic: evidence from poly(3-hydroxybutyrate-co-3-hydroxyhexanoate). *Environ. Sci. Technol.* **55**, 3380–3388 (2021).
65. Queiroz, S. S., Jofre, F. M., Mussatto, S. I. & Felipe, M. G. A. Scaling up xylitol bioproduction: challenges to achieve a profitable bioprocess. *Renew. Sustain. Energy Rev.* **154**, 111789 (2022).
66. DuChanois, R. M. et al. Prospects of metal recovery from wastewater and brine. *Nat. Water* **1**, 37–46 (2023).
67. Ross, D. E., Flynn, J. M., Baron, D. B., Gralnick, J. A. & Bond, D. R. Towards electrosynthesis in *Shewanella*: energetics of reversing the Mtr pathway for reductive metabolism. *PLoS ONE* **6**, e16649 (2011).
68. Okamoto, A., Hashimoto, K. & Nealson, K. H. Flavin redox bifurcation as a mechanism for controlling the direction of electron flow during extracellular electron transfer. *Angew. Chem. Int. Ed.* **53**, 10988–10991 (2014).
69. Rowe, A. R. et al. Tracking electron uptake from a cathode into *Shewanella* cells: Implications for energy acquisition from solid-substrate electron donors. *mBio* **9**, e02203-17 (2018).
70. Lu, Z., Jiang, K., Chen, G., Wang, H. & Cui, Y. Lithium electrochemical tuning for electrocatalysis. *Adv. Mater.* **30**, 1800978 (2018).
71. Hunter, J. C. Preparation of a new crystal form of manganese dioxide: λ-MnO_2. *J. Solid State Chem.* **39**, 142–147 (1981).
72. Varma, A., Mukasyan, A. S., Rogachev, A. S. & Manukyan, K. V. Solution combustion synthesis of nanoscale materials. *Chem. Rev.* **116**, 14493–14586 (2016).
73. Shimokawa, K., Matsubara, S., Okamoto, A. & Ichitsubo, T. Light-induced Li extraction from $LiMn_2O_4/TiO_2$ in a water-in-salt electrolyte for photo-rechargeable batteries. *Chem. Commun.* **58**, 9634–9637 (2022).
74. Ramana, C. V., Mauger, A., Gendron, F., Julien, C. M. & Zaghib, K. Study of the Li-insertion/extraction process in $LiFePO_4/FePO_4$. *J. Power Sources* **187**, 555–564 (2009).
75. Momma, K. & Izumi, F. VESTA 3 for three-dimensional visualization of crystal, volumetric and morphology data. *J. Appl. Crystallogr.* **44**, 1272–1276 (2011).
76. Izumi, F. & Momma, K. Three-dimensional visualization in powder diffraction. *Solid State Phenom.* **130**, 15–20 (2007).
77. Peters, J. F. Best practices for life cycle assessment of batteries. *Nat. Commun.* **6**, 614–616 (2023).
78. Kelly, J. C., Wang, M., Dai, Q. & Winjobi, O. Energy, greenhouse gas, and water life cycle analysis of lithium carbonate and lithium hydroxide monohydrate from brine and ore resources and their use in lithium ion battery cathodes and lithium ion batteries. *Resour. Conserv. Recycl.* **174**, 105762 (2021).
79. Huijbregts, M. A. J. et al. ReCiPe, R. I. V. M.: In a harmonized life cycle impact assessment method at midpoint and endpoint level report I: characterization. *National Institute for Public Health and the Environment: Bilthoven, The Netherlands*. 1–194 (2016).
80. Tian, X., Richardson, R. E., Tester, J. W., Lozano, J. L. & You, F. Retrofitting municipal wastewater treatment facilities toward a greener and circular economy by virtue of resource recovery: Techno-economic analysis and life cycle assessment. *ACS Sustain. Chem. Eng.* **8**, 13823–13837 (National Institute for Public Health and the Environment, 2020).

Acknowledgements

The authors thank Dr. Takashi Fujikawa, Dr. Fuyuki Sakamoto, and Dr. Akio Iwanade for their technical help with the materials synthesis and ICP-MS/OES analysis. We also thank Prof. Tetsu Ichitsubo (Tohoku University) and Prof. Michael De Volder (University of Cambridge) for fruitful discussions. This research was supported by NIMS Joint Research Hub Program (QN3510) and by JSPS KAKENHI (Grant Number: 22H02265 (A.O.), 20K22460 (K.S.)) and JST, PRESTO (Grant Number: JPMJPR19H1 (A.O.)), Japan. XRD, SEM–EDS, FIB–SEM–EDS, and STEM–EELS analyses were carried out at the NIMS Battery Research Platform. ICP-MS/OES analysis was performed at Materials Analysis Station, NIMS, and at Analytical Research Core for Advanced Materials, Institute for Materials Research, Tohoku University. A part of this work was supported by Advanced Research Infrastructure for Materials and Nanotechnology in Japan (ARIM) of the Ministry of Education, Culture, Sports, Science and Technology (MEXT) (Grant Number: JPMXP1224NM5295).

Author contributions

K.S., D.M.P., and A.O. conceived and designed this study. A.O. supervised the project. K.S. and D.M.P. conducted materials synthesis and characterization. K.S., D.M.P., and X.L. carried out Li recovery from PBS and seawater. D.M.P., H.Y.T., and Y.K. performed TEA/LCA. K.S., D.M.P., and A.O. wrote the first draft, and all authors participated in the manuscript revision.

Competing interests

Research funding related to pilot-scale Li-recovery trials was received from two industrial partners; these partners were not involved in the present study. The authors also hold non-financial collaborations on large-scale MnO_2 production and brine testing; no materials from these collaborations were used in this study. K.S., D.M.P., and A.O. filed a patent application for the bioelectrochemical Li recovery method to the Japanese patent office (patent number 7755348). All other authors declare no competing interests.

Additional information

Supplementary information The online version contains supplementary material available at https://doi.org/10.1038/s41467-026-74500-3.

Correspondence and requests for materials should be addressed to Kohei Shimokawa, Yasunori Kikuchi or Akihiro Okamoto.

Peer review information *Nature Communications* thanks the anonymous reviewers for their contribution to the peer review of this work. A peer review file is available.

Reprints and permissions information is available at http://www.nature.com/reprints

Publisher's note Springer Nature remains neutral with regard to jurisdictional claims in published maps and institutional affiliations.

Open Access This article is licensed under a Creative Commons Attribution-NonCommercial-NoDerivatives 4.0 International License, which permits any non-commercial use, sharing, distribution and reproduction in any medium or format, as long as you give appropriate credit to the original author(s) and the source, provide a link to the Creative Commons licence, and indicate if you modified the licensed material. You do not have permission under this licence to share adapted material derived from this article or parts of it. The images or other third party material in this article are included in the article's Creative Commons licence, unless indicated otherwise in a credit line to the material. If material is not included in the article's Creative Commons licence and your intended use is not permitted by statutory regulation or exceeds the permitted use, you will need to obtain permission directly from the copyright holder. To view a copy of this licence, visit http://creativecommons.org/licenses/by-nc-nd/4.0/.

© The Author(s) 2026